Computerized Medical Imaging and Graphics 56 (2017) 60–73

Contents lists available at ScienceDirect

Computerized Medical Imaging and Graphics

journal homepage: www.elsevier.com/locate/compmedimag

Plantar fascia segmentation and thickness estimation in ultrasound images

Abdelhafid Boussouar[a,*], Farid Meziane[a], Gillian Crofts[b]

[a] School of Computing, Science and Engineering, University of Salford, Salford, Manchester M6 6PU, United Kingdom
[b] School of Health Sciences, University of Salford, Salford, Manchester M5 4WT, United Kingdom

ARTICLE INFO

Article history:
Received 7 September 2016
Received in revised form 9 January 2017
Accepted 13 February 2017

Keywords:
Ultrasound (US)
Speckle noise
Plantar fascia (PF)
Segmentation
Radial Basic Function Neural Network (RBF-NN)
Feature extraction
Classification

ABSTRACT

Ultrasound (US) imaging offers significant potential in diagnosis of plantar fascia (PF) injury and monitoring treatment. In particular US imaging has been shown to be reliable in foot and ankle assessment and offers a real-time effective imaging technique that is able to reliably confirm structural changes, such as thickening, and identify changes in the internal echo structure associated with diseased or damaged tissue. Despite the advantages of US imaging, images are difficult to interpret during medical assessment. This is partly due to the size and position of the PF in relation to the adjacent tissues. It is therefore a requirement to devise a system that allows better and easier interpretation of PF ultrasound images during diagnosis. This study proposes an automatic segmentation approach which for the first time extracts ultrasound data to estimate size across three sections of the PF (rearfoot, midfoot and forefoot). This segmentation method uses artificial neural network module (ANN) in order to classify small overlapping patches as belonging or not-belonging to the region of interest (ROI) of the PF tissue. Features ranking and selection techniques were performed as a post-processing step for features extraction to reduce the dimension and number of the extracted features. The trained ANN classifies the image overlapping patches into PF and non-PF tissue, and then it is used to segment the desired PF region. The PF thickness was calculated using two different methods: distance transformation and area-length calculation algorithms. This new approach is capable of accurately segmenting the PF region, differentiating it from surrounding tissues and estimating its thickness.

1. Introduction

The plantar fascia (PF) or plantar aponeurosis is an aponeurotic thick, fibrous and strong connective tissue that provides stability to the medial longitudinal arch of the foot (Huang et al., 1993). It originates at the medial calcaneal tuberosity and extends toward the digits in three different structural bands: medial, central, and lateral (Chang, 2010) (Fig. 1). The central area is the largest, most affected by disease and most susceptible to deformities (Kwong et al., 1988; Kelikian, 2012). The PF plays an important role in stabilizing the foot during walking and running. However, a commonly encountered condition is foot pain due to overuse. The assessment of foot pain typically involves clinical examination and diagnostic imaging Park et al. (2014). The role of diagnostic imaging is to provide objective information which significantly then informs clinical decisions on treatment options. Ultrasound (US) imaging is a real-time imaging technique used in the diagnosis of the PF, which is readily available, fast, causes no radiation exposure, portable, accurate, and cost-effective (Pope, 1999; Szabo, 2013). Moreover, it is considered highly reliable and favourable in the diagnosis of diabetic foot with plantar fasciitis, ankle infections and damaged soft tissue (Crofts et al., 2014; Angin et al., 2014; Szabo, 2013; Akfirat et al., 2003). Although US imaging offers many advantages in the diagnosis of PF conditions, it is often considered operator dependent when used by non-experts. In addition, the quality of images may be affected by the presence of speckle noise (Ganzalez and Woods, 2002) which may diffuse the image edges, making medical interpretation and biometric measurements challenging, and therefore impacting the accuracy of diagnosis.

Research has reported thickening and hypoechoic deformities of the PF as part of the diagnostic criteria and PF characteristic features (Park et al., 2014). Increased PF thickness of >4 mm and decreased PF echogenicity are considered symptomatic (Fabrikant

---

[*] Corresponding author.
E-mail addresses: a.boussouar1@edu.salford.ac.uk (A. Boussouar), f.meziane@salford.ac.uk (F. Meziane), g.crofts@salford.ac.uk (G. Crofts).

http://dx.doi.org/10.1016/j.compmedimag.2017.02.001
0895-6111/© 2017 Published by Elsevier Ltd.

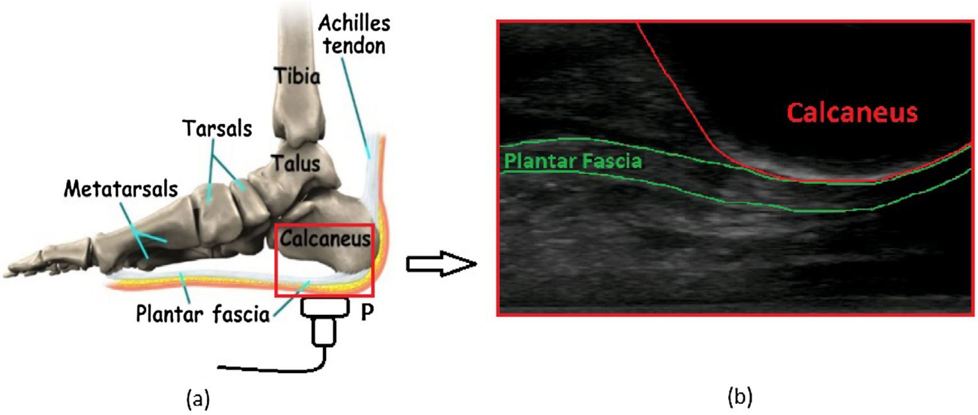

Fig. 1. Plantar fascia region: (a) Anatomical illustration diagram showing the anatomical location of the plantar fascia and positioning of the US probe, P. (b) The longitudinal sonogram of the scanned region related to (a), showing the plantar fascia area and the calcaneus.

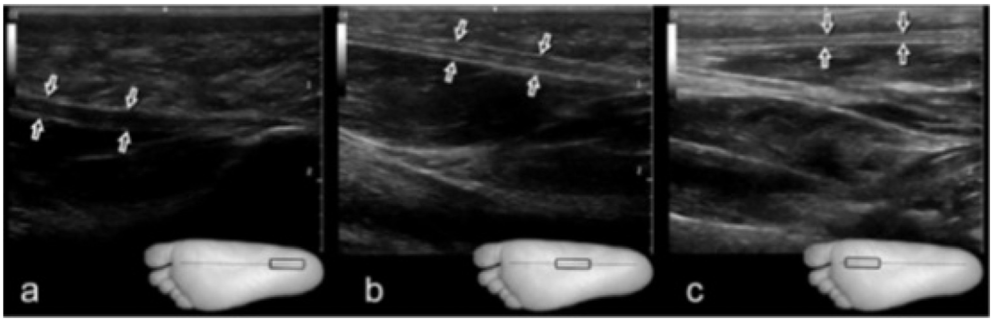

Fig. 2. Probe position, longitudinal orientation and sample US images for all PF different structures. (a) Rear PF section; (b) Mid PF section; and (c) Forefoot PF section.

and Park, 2011; Wearing et al., 2007; Saber et al., 2012). Different protocols are used in the literature to manually measure PF thickness: (1) PF measurement has primarily been limited to thickness at the insertion of the calcaneus with either inter- or intra-rater reliability (Cheng et al., 2012); (2) average bias of repeated PF measurements (Wearing et al., 2004); (3) recent work (Crofts et al., 2014) has shown that the PF thickness varies along its length. Therefore, a reliable means of quantifying PF thickness in different sites (rearfoot, midfoot and forefoot) is advantageous (Fig. 2).

Automatic segmentation is one of the most critical tasks in medical image analysis; it is mainly used to locate region of interest (ROI) objects and boundaries in images. It is considered the most challenging task in medical US imaging compared to other imaging modalities, such as CT and MRI due to attenuation, speckles, shadows, signal loss and drop-out.

Furthermore, there is no commonly accepted method for US image segmentation because segmentation techniques vary widely according to the specific problem, application, imaging modality, human interaction, the homogeneity of images, spatial characteristics of images, continuity, texture and image content (Noble and Boukerroui, 2006; Rueda et al., 2014). Although many segmentation methods and techniques of US images exist, there is little literature on the segmentation process of the plantar fascia in US images of the foot. The only previous work found in relation to PF tissue US images is that reported in (Deshpande et al., 2013) using the Chan-Vese active contour segmentation method (Chan and Vese, 2001). The Chan-Vese model is based on the variational information in grayscale intensities of the image. This proposed technique was effective in the detection of bones and in segmenting the soft tissue layers between the bone and the skin in US images of the foot. However, this method is used for segmenting the whole plantar tissue without defining different plantar tissue areas. Most active contour methods used in US images suffer from the following shortcomings that seriously affect the segmentation results (Chang et al., 2010): (1) these methods are sensitive to the edge gradient; (2) they need a clear definition of the initial contour mask; (3) they depend on the number of iterations which may affect segmentation accuracy; and (4) they suffer from a high level of computational complexity. Many researchers have made various improvements to the standard active contour, but the disadvantages of this method are still not fundamentally overcome.

Artificial neural network (ANN) techniques have attracted considerable attention in medical imaging due to its intelligence and learning capabilities of performing complicated tasks such as US segmentation and classification. Previous studies (Chang et al., 2010; Noble and Boukerroui, 2006) have shown that integration of ANN can facilitate and improve the segmentation process. Fig. 3 illustrates how ANNs can be used to segment the ROI of US images. In general, ANNs supervised segmentation approaches consist of following steps: (1) the input images are divided into different overlapping patches; (2) different sets of features are calculated on these image patches and then selected to reduce their redundancy; (3) the selected feature vectors are then presented as input vectors to the trained ANN (trained previously with a set of ground truth segmentation, performed manually by experts) where the image patches are classified as a part of either the background or the ROI; (4) the results of the image patches classification are then combined and merged into a region mask (in black and white colour for background and ROI, respectively); (5) region mask labelling and superposing.

The manual segmentation and analysis of the large PF US datasets is a tedious, time-consuming and complex task for

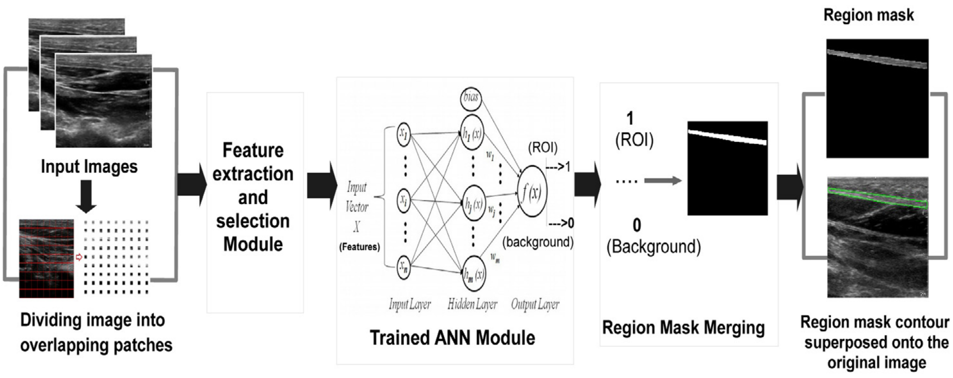

Fig. 3. Block diagram showing ANNs approach to segmenting ROIs.

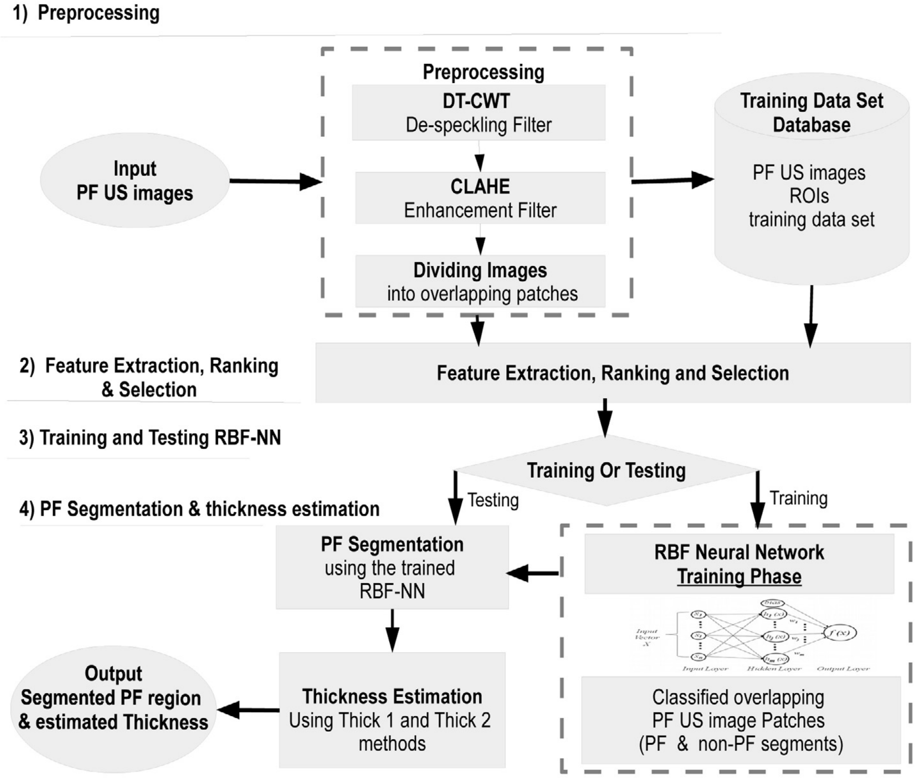

Fig. 4. Plantar fascia segmentation and thickness estimation in ultrasound images approach.

physicians and clinicians, who have to manually select the ROIs and extract useful diagnostic information. This analysis will lead to inter- or intra-operator variability errors. Motivated by the advantages offered by ANN approaches, we propose a general segmentation ANN-based approach that uses the Radial Basic Function Neural Network (RBF-NN) classifier (Ham and Kostanic, 2000) to automatically segment, estimate PF thickness, to improve PF US data analysis and to assist doctors in qualitative diagnosis. Six different textual feature sets extracted from the ROI are used to train the RBF-NN. The trained RBF-NN classifies PF patches into PF ROIs and background (non-PF), and then is used to segment the PF region. PF thickness is calculated using two different approaches: distance transformation and area-length calculation. This is, to our knowledge, the first segmentation method in the plantar fascia US imaging field. Therefore, accuracy of the technique at this stage is an important step to facilitate the success of the classification process during clinical diagnosis.

2. Proposed plantar fascia segmentation and thickness estimation model

The proposed model consists of the following steps as illustrated in Fig. 4: (1) preprocessing: during this stage, speckle noise reduction and enhancement filters are applied, then images are divided into small overlapping patches; (2) feature extraction, ranking and selection (feature analysis): in this stage, 32 different features are extracted from the ROIs training dataset and analysed so that they are more prominent and suitable for RBF-NN classifier using feature ranking and selection techniques; (3) training and testing RBF-NN: the RBF neural network classifier is trained using the selected training dataset and classifies the overlapping patches to PF and non-PF regions; (4) PF segmentation and thickness estimation: segmentation is carried out using the trained RBF-NN and PF thickness is calculated using two methods; (a) distance transformation with

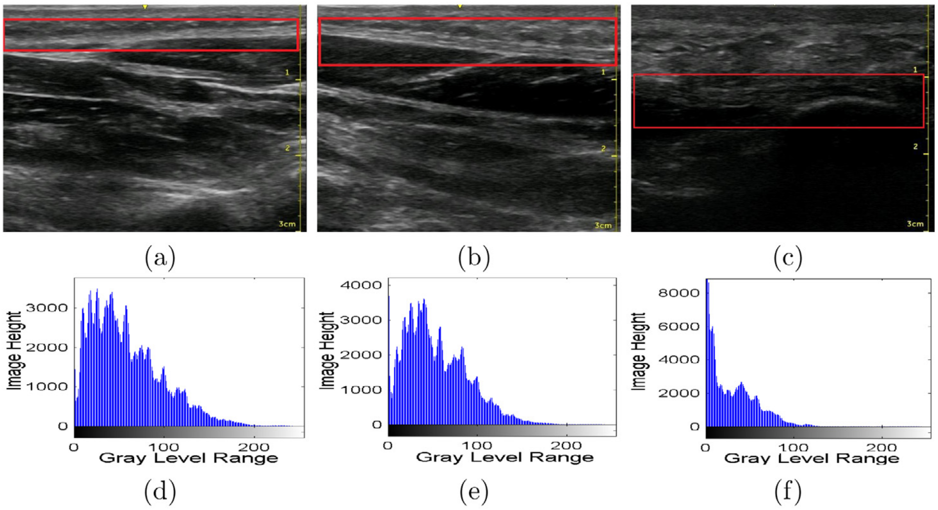

(a) (b) (c)

(d) (e) (f)

Fig. 5. (a)–(c) US images for different PF structures: (a) Forefoot, (b) Midfoot and (c) Rearfoot section. (d)–(f) Gray level histogram representation.

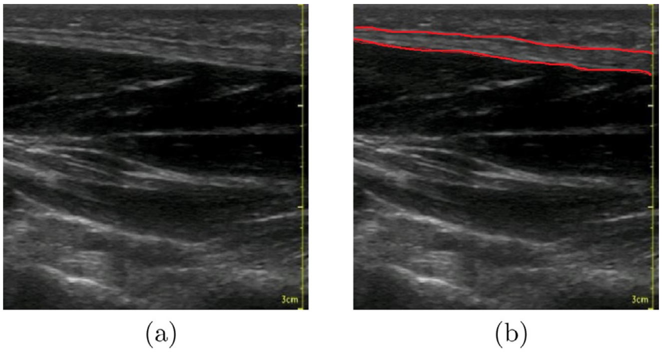

(a) (b)

Fig. 6. (a) Original image and (b) Targeted PF region selected by a physician (red contours).

median calculation and (b) average thickness expressed as PF area divided by PF length.

2.1. PF US image acquisition and tools

Different plantar fascia US images, scanned from a patient's footprint area (in the prone position) were used in this study (Fig. 5); 150 different real US images were collected from 25 patients to compare the presented methods (6 PF US images per patient for different PF structures rearfoot, midfoot and forefoot sections) with 256 gray levels, a size dimension of 600 × 655 pixels and a resolution of 28.35 pixels/centimeter. All the proposed method stages were implemented using Matlab R2016a (The MathWorks Inc., Natwick, USA).

These images were obtained from the Health Sciences Department, University of Salford, acquired by two expert clinicians according to a precise protocol using a portable Venue 40 musculoskeletal US system (GE Healthcare, UK) with a $5-13$ MHz wideband linear array probe (12.7 mm × 47.1 mm). The thickness of the PF was measured manually (Fig. 6) at three different sites: rearfoot, midfoot and forefoot sections.

2.2. Preprocessing

The presence of speckle noise in medical US images is a very common, undesirable feature as it significantly degrades image quality, thereby decreasing the efficiency and reliability of medical image processing tasks, such segmentation and feature extraction. Thus, despeckling and enhancement preprocessing steps are employed to reduce noise and improve the visual quality of the acquired PF images, followed by dividing the images into overlapping patches. Preprocessing steps are described in more detail in the following sub-sections.

2.2.1. Dual-tree complex wavelet transform (DT-CWT) filter

Motivated by the advantages of DT-CWT (Kingsbury, 1998), a dual tree complex wavelet transform filter was applied before the CLAHE algorithm to reduce speckle noise, enhance PF images and avoid noise amplification in US images. This filter integrates homomorphic transformation and multi-scale DT-CWT to reduce speckle noise in US images. Implementation details of the DT-CWT can be found in (Kingsbury, 1998, 1999; Selesnick et al., 2005). The despeckling filter consists of the following steps: (a) homomorphic transformation; (b) DT-CWT image decomposition; (c) threshold estimation, modification and suppression of noisy coefficients using BayesShrink thresholding rule (Chang et al., 2000) and bivariate function (Sendur and Selesnick, 2002); (d) application of inverse DT-CWT for signal composition; and (e) exponential transformation to obtain despeckled signal.

2.2.2. Image enhancement using contrast-limited adaptive histogram equalization (CLAHE)

In medical imaging, CLAHE (Zuiderveld, 1994) is advantageous in enhancement of low-contrast images when compared to standard adaptive histogram equalization (AHE) (Pizer et al., 1987); where the histogram is calculated for the contextual region of a pixel. In this work, the CLAHE enhancement was performed to adjust the intensity of the PF region using different steps as described in Zuiderveld (1994).

2.3. Feature extraction

PF area has a reasonably defined structure, with the most common characteristic being its thickness and texture; therefore, features extracted in this work were used to define the shape of the PF region precisely. A total of 6 different texture feature sets were extracted from the overlapping patches (32 features for each): (i) Histogram features (Umbaugh, 2005): (1) mean, (2) standard deviation, 3) skewness, (4) energy, and (5) entropy. (ii) Haar wavelet features (Wen et al., 2007): (1) mean and (2) variance haar wavelet features (Gonzalez and Woods, 2011) of the low-low (LL) frequency sub-band. (iii) Block-difference of inverse probabilities

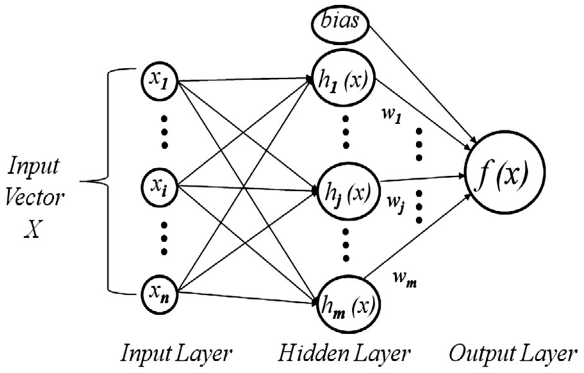

Fig. 7. A graphical representation of RBF-NN architecture.

feature (BDIP): to assess variations in local brightness (Chun et al., 2003). (iv) Gray level difference statistics (GLDS) (Weszka et al., 1976): (1) contrast, (2) angular second moment, (3) entropy, and (4) mean. In this work, GLDS were computed for the following displacements: $\delta = (0, 1), (1, 1), (1, 0), (1, -1)$, where $\delta \equiv (\Delta x, \Delta y)$ and their average values were calculated. (v) Haralick spatial gray level dependence matrices (SGLDM) (Haralick et al., 1973): (1) angular second moment, (2) contrast, (3) correlation, (4) sum of squares, (5) variance, (6) inverse difference moment (InvDiffMoment), (7) sum average, (8) sum variance, (9) sum entropy, (10) entropy, (11) difference variance, (12) difference entropy, and (13) information measures of correlation. The above SGLDM features were calculated and averaged for a selected distance $d = 1$ (3×3 matrices) and four different orientation angles $\theta = 0$ deg, 45 deg, 90 deg, and 135 deg. (vi) Region based features: (1) area, (2) perimeter, (3) major axis length, (4) minor axis length, (5) equivalent diameter, (6) extent, and (7) convex area.

2.4. Feature ranking and selection

A common problem in most classification processes is the large number of extracted features compared to the number of observations, leading to over-fitting. There were 32 features extracted from each PF patch, some of which may be correlated, redundant or not useful. Therefore, a feature ranking and selection technique was used to reduce correlated measurements and to select the most discriminating parameters; an unsupervised filter-based feature (Infinity feature) selection method (Roffo et al., 2015). Only 15 features were chosen as reported in Section 4.1.

2.5. Radial basis function neural network (RBF-NN)

RBF-NN (Broomhead and Lowe, 1988; Moody and Darken, 1989) has been widely used in the field of pattern recognition and digital image processing due to its simplicity, functional approximation, interpolation and generalization capabilities (Borş and Pitas, 1999). The RFB-NN was designed as a three-layer feed-forward neural network topology: an input layer feeding the feature vectors into the RBF-NN; a hidden layer with radial basis function as activation function and high dimensionality structure; and an output layer where all the adjacent layer nodes were fully connected and the linear combination of the hidden weighted radial basis functions was calculated Orr (1996). In the PF segmentation process, the selected features of overlapping patches were applied to the previously trained RBF-NN as input vectors in order to classify the PF images into PF and non-PF regions. The architecture of RBF-NN model is graphically illustrated in Fig. 7.

The output of a RBF-NN model can be calculated by the following equation:

$$f(x) = \sum_{j=1}^{m} w_j h_j(x) + B_k W_k, \; k = 1, 2, \ldots, m, \qquad (1)$$

where $x \in R^n$ is an input feature vector, $h_j(x)$ is the basis function of the network from R^n to R, m is the number of hidden units in the hidden layer, and w_j values are weights of the network, B_k and W_k are the unit positive bias and weight from the bias neuron, respectively (an extra basis function whose output is fixed at 1 serves as the bias for each output unit). A Gaussian function Borş and Pitas (1996) and Stochastic gradient-based supervised learning strategy were used to update all parameters of RBF-NN, including the radial basis function centers, the widths of the Gaussian radial basis functions, and the output weights. The error cost on the input/output pattern of the RBF feed-forward neural networks can be calculated using the following equation:

$$E(x) = \frac{1}{2}[t(x) - f(x)]^2, \qquad (2)$$

where $x \in R^n$ is an input vector, $t(x) \in \{0, 1\}$ is the corresponding target output, $f(x)$ is the actual output defined by equation (1).

2.5.1. Training and testing the RBF neural network

The RBF-NN was created as one-hidden-layer feed-forward neural network topology with 20 hidden nodes determined experimentally based on the minimum mean square error, with radial basis function as activation function, and one output layer. The proposed RBF-NN segmentation method was applied on all PF ultrasound images. The PF images were divided into small overlapping patches of size 9×9 and overlap of 4.5 pixels, where their features were extracted. The selected feature vectors were regarded as the input vectors of the RBF-NN classifier. In the classification process, the convergence conditions of the RBF-NN were set to 10^4 for maximum progress epochs and less than 10^{-5} for the correction value of synaptic weights. When one of these conditions was satisfied, the training process was terminated. The neural network model was tuned using the k-fold with ‘leave-one-out’ cross-validation approach where k is equal to the total number of selected features (Bishop, 2006), and the input and target vectors is automatically split into training, validation, and testing samples. For the training record, we used 60% for training, 20% for testing, and 20% for validation. A total of 300 training patterns (150 PF and 150 non-PF region textures) extracted by experienced physicians were used to train the RBF-NN. The training process continued until validation improvement was achieved. The testing data provided a separate measure of RBF-NN accuracy. 60 PF US images were used to create the testing dataset.

2.5.2. Segmentation of plantar fascia region using RBF

The next step was to analyse and trace the PF region of the US images using the connected component labeling algorithm presented in (Di Stefano and Bulgarelli, 1999; Gonzalez et al., 2010). This algorithm is used to assign or divide each PF component based on the image boundaries function using 4 or 8-connectivity; 8-connected neighbourhood connectivity was used to trace and label the PF region. The largest connected components extracted from the classified PF US image were considered as a part of the PF area. In the labeling algorithm process, seed equivalences were processed directly in the initial scan so that classes sharing the same set of intensity values were always sorted and updated at once during the first scan. This is maintained by assigning a unique new label to each new equivalence class and merging the corresponding classes as soon as a new equivalence is determined.

Table 1
Intra- and inter-operator variability of manual segmentation of PF structure.

Metrics	Region based metrics					Distance based metrics	
	Accuracy (%)	Precision (%)	Sensitivity (%)	Specificity (%)	Dice (%)	Hausdorff (mm)	MSSD (mm)
Intra-operator differences							
Operator 1	98.08 ± 2.07	97.87 ± 1.07	95.97 ± 1.45	99.10 ± 1.18	96.65 ± 1.60	2.26 ± 1.62	0.66 ± 0.81
Operator 2	98.01 ± 2.00	97.65 ± 1.80	95.14 ± 1.95	98.94 ± 1.54	96.35 ± 1.69	2.41 ± 1.80	0.42 ± 0.56
Inter-operator differences							
Operator 1 ***vs*** Operator 2	98.06 ± 1.81	97.77 ± 1.25	95.73 ± 1.62	98.87 ± 1.34	96.89 ± 2.61	2.78 ± 1.56	0.74 ± 0.64
Linear regression analysis	R^2	0.92	P	<0.0001			
Paired t-test	P	0.853					

Table 2
Feature selection analysis results of the best 15 extracted features.

Feature no.	Selected feature sets	Predictor importance weight	Predictor rank order
Haar wavelet			
1	HaarVariance	7.549	5
2	HaarMean	5.789	15
Gray level difference statistics (GLDS)			
10	Contrast	6.081	10
11	Correlation	6.038	11
12	Energy	5.802	14
13	Homogeneity	6.195	7
Spatial gray level dependence matrices (SGLDM)			
15	Contrast	23.775	1
16	Correlation	6.116	9
17	SumofSquares	12.225	3
19	InvDiffMoment	5.892	12
20	SumAverage	17.426	2
23	DifferenceVariance	9.092	4
Region Based Features			
27	Area	5.831	13
28	Perimeter	6.293	6
29	MajorAxisLength	6.136	8

2.6. PF thickness measurement and estimation

The PF thickness estimation process is summarized in the following methods: (a) Thick 1 method: (1) distance transformation was applied to the segmented PF US image using Euclidean distance metric (Shih, 2009), so that all background pixels were set to 0 and all foreground pixels were set to the distance from the background; (2) the local maxima pixel set points (spot centers) of the distance transformed segmented PF image were found (i.e. distances from the background). These local maxima points are also known as skeleton centered points (ridges) (Blum, 1967) with respect to the shape boundary (Telea, 2014); and (3) the thickness was computed as the median of the local maxima pixel set points. (b) Thick 2 method: For each PF US segment, we computed the following parameters using property measures of the PF region and morphological operations (Ganzalez and Woods, 2002): (1) the area as the total number of pixels in the PF binary image region; (2) the length of the PF using morphological operations on the PF binary region, such as remove and skeleton; and (3) the mean PF thickness was computed as PF area divided by PF length.

The calculated PF thickness using Thick 1 and Thick 2 methods was compared against manual clinical measurements to assess the performance of the developed methods. All thickness measurements were reported in millimetres (mm). All the images used were 3 cm deep, which translated to a conversion of 1 cm for 156 pixels.

2.7. Alternative methods used for performance comparisons

Due to the absence of different automatic segmentation methods in the PF US imaging field, the proposed method was compared with only two different region based active contour segmentation methods: (1) semi-automated active contour model (snakes) by Kass et al. (1988), incorporating different active contour energy factors; and (2) automated localizing region based active contour method by Lankton and Tannenbaum (2008). Both methods are based on the variational information of grayscale intensities of the image, and they performed poorly when there was no much difference between the foreground and background means, especially in PF US images. In order to increase the variation information of the grayscale intensities in the US images, we introduced two different stages to tune and initialize the parameters of the images: (1) preprocessing was performed using (a) contrast limited adaptive histogram equalization (CLAHE), (b) manual and automatic initial contour mask initialization; and (c) definition of the number of iterations; (2) applying morphological operations (Ganzalez and Woods, 2002), such as (a) opening, closing, thresholding, in order to remove falsely identified small segments (usually due to image speckle noise and small variation in image intensities), (b) region filling and labeling, where the final segmented area was filled and labeled. For the first method (semi-automatic), the initial contour mask was defined manually by selecting a random set of points near PF ROIs which were later interpolated into a contour. The iteration number was set experimentally to 100, and images were resized to 1/2 the original size for fast computation. In the second method, the active contour was automatically initialized using a predefined initial mask (4-element vector) for different PF US images and the iteration number was set experimentally to 800.

Table 3
The performance measures of the RBF-NN classifier using different selected feature sets. The bold font represents the best performing number of features.

Feature sets	Accuracy	TNR	CE
Best (5) Selected Features	98.735	99.3650	0.115
Best (10) Selected Features	98.736	99.3660	0.090
Best (15) Selected Features	**98.751**	**99.3720**	**0.018**
Best (20) selected features	98.750	99.3717	0.058
All (32) features	98.741	99.3700	0.083

3. Performance evaluation protocol

3.1. Classification evaluation

Different performance metrics were used to evaluate the performance of the RBF-NN classifier: accuracy, true negative rate (TNR) (Sokolova and Lapalme, 2009), and cross-entropy error (CE) (Rubinstein, 1997). These measures are defined as follows:

$$Accuracy = \frac{TP + TN}{N}, \tag{3}$$

$$TNR = \frac{TN}{TN + FP}, \tag{4}$$

$$CE(X, Y) = -\frac{1}{N}\sum_{i=1}^{n} y^{(i)} \ln(a(x^{(i)}) + (1 - y^{(i)}) \ln(1 - a(x^{(i)})), \tag{5}$$

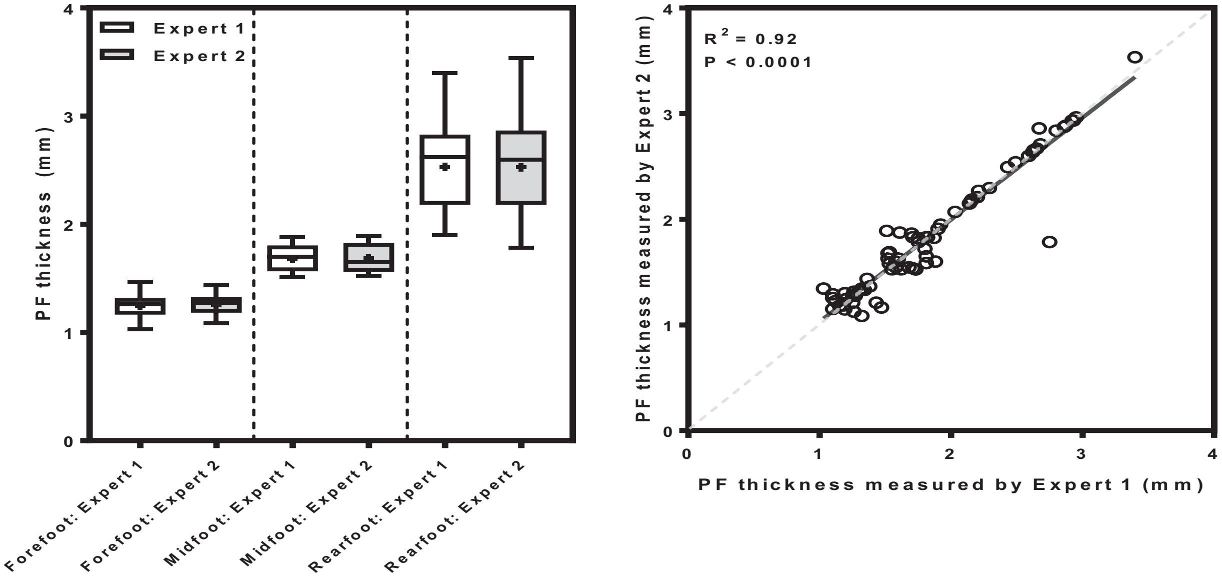

(a)

(b)

Fig. 8. Inter-operator variability: (a) differences in thickness measurements of PF structures performed by the two experts, indicating lack of differences. The boxes show the 25th and the 75th percentiles, the whiskers denote the minimum and maximum values, the bars represent the medians, the + sign represents the means. (b) Linear regression of measurements performed by the two experts, indicating consistent pairing. The dashed line represents the line of unity and the continuous line represents the line of regression ($R^2 = 0.92$).

where *TP* and *TN* represent true positive and true negative values, respectively, calculated from a confusion matrix, *N* is the total number of all values in the confusion matrix classes including: TP, TN, FP (false positive), and FN (false negative). TNR represents specificity (the probability of the correctly classified non-positive elements as predicted negative). $X = x^{(1)}, \ldots, x^{(n)}$ is the set of input selected features in the training dataset, and $Y = y^{(1)}, \ldots, y^{(n)}$ is the set of corresponding labels for input features. The $a(x)$ represents the output of the neural network for the given input feature set x.

3.2. Segmentation evaluation

Two different quantitative evaluation metrics found in the literature were considered to evaluate the segmentation method including region-based metrics (area overlap measures) (Udupa et al., 2006) and distance based metrics (Heimann et al., 2009). Their mathematical representations are summarized below.

3.2.1. Region based metrics

Region based performance metrics Udupa et al. (2006), Rueda et al. (2014) are used to calculate precision, Dice similarity Dice (1945) and accuracy (using sensitivity and specificity) of the proposed segmentation method. These metrics are defined as follows:

$$Precision = \frac{\left|S_r \cap R_{gt}\right|}{\left|S_r \cup R_{gt}\right|}, \tag{6}$$

$$Dice = \frac{2\left|S_r \cap R_{gt}\right|}{\left|S_r + R_{gt}\right|}, \tag{7}$$

$$Sensitivity = \frac{\left|S_r \cap R_{gt}\right|}{\left|R_{gt}\right|}, \tag{8}$$

$$Specificity = \frac{\left|S_r \cup R_{gt}\right|}{\left|R_{gt}\right|}, \tag{9}$$

where S_r denotes the segmented results, R_{gt} represents the reference ground truth image defined by experts, $|.|$ denotes the magnitude, $\cap$ denotes the intersection (the number of common pixels in both segmented results and ground truth), and $\cup$ is the union (the number of all ground truth pixels defined by expert and the segmented results).

3.2.2. Distance based metrics

Different distance-based metrics Heimann et al. (2009), Rueda et al. (2014) were applied including Hausdorff and mean sum of square distance (MSSD) metrics. These metrics are defined as follows:

(1) Hausdorff distance, also known as maximum symmetric contour distance (MSD), is defined as:

$$MSD(R_{gt}, S_r) = \max((D_1(C_{R_{gt}}, C_{S_r}), D_1(C_{S_r}, C_{R_{gt}})), \tag{10}$$

where $C_{R_{gt}}$ and C_{S_r} denote the reference ground truth contour and segmented result contour of R_{gt} and S_r, respectively. $D_1(C_{R_{gt}}, C_{S_r})$ and $D_1(C_{S_r}, C_{R_{gt}})$ can be calculated using Euclidean distance as follows:

$$D_1(C_{R_{gt}}, C_{S_r}) = \max_{x_1 \in C_{R_{gt}}}(\min_{x_2 \in C_{S_r}}(\|x_1 - x_2\|)) \tag{11}$$

$$D_1(C_{S_r}, C_{R_{gt}}) = \max_{x_2 \in C_{S_r}}(\min_{x_1 \in C_{R_{gt}}}(\|x_2 - x_1\|)) \tag{12}$$

where x_1, x_2 denote the contour elements of C_{S_r} and R_{gt}, respectively, and $\|.\|$ represents the Euclidean distance.

(2) The MSSD is defined by:

$$MSSD(R_{gt}, S_r) = \frac{1}{N}\sum_{n=1}^{N} D_2^2(C_{R_{gt}}, C_{S_r}(x_n)), \tag{13}$$

where *N* denotes the size of the segmented result contour, $C_{R_{gt}}$ and C_{S_r} represent the reference ground truth contour and segmented result contour of R_{gt} and S_r, respectively. $D_2(C_{R_{gt}}, C_{S_r})$ can be calculated using:

$$D_2(C_{R_{gt}}, C_{S_r}(x)) = \min_{y \in R_{gt}}(\|y - x\|) \tag{14}$$

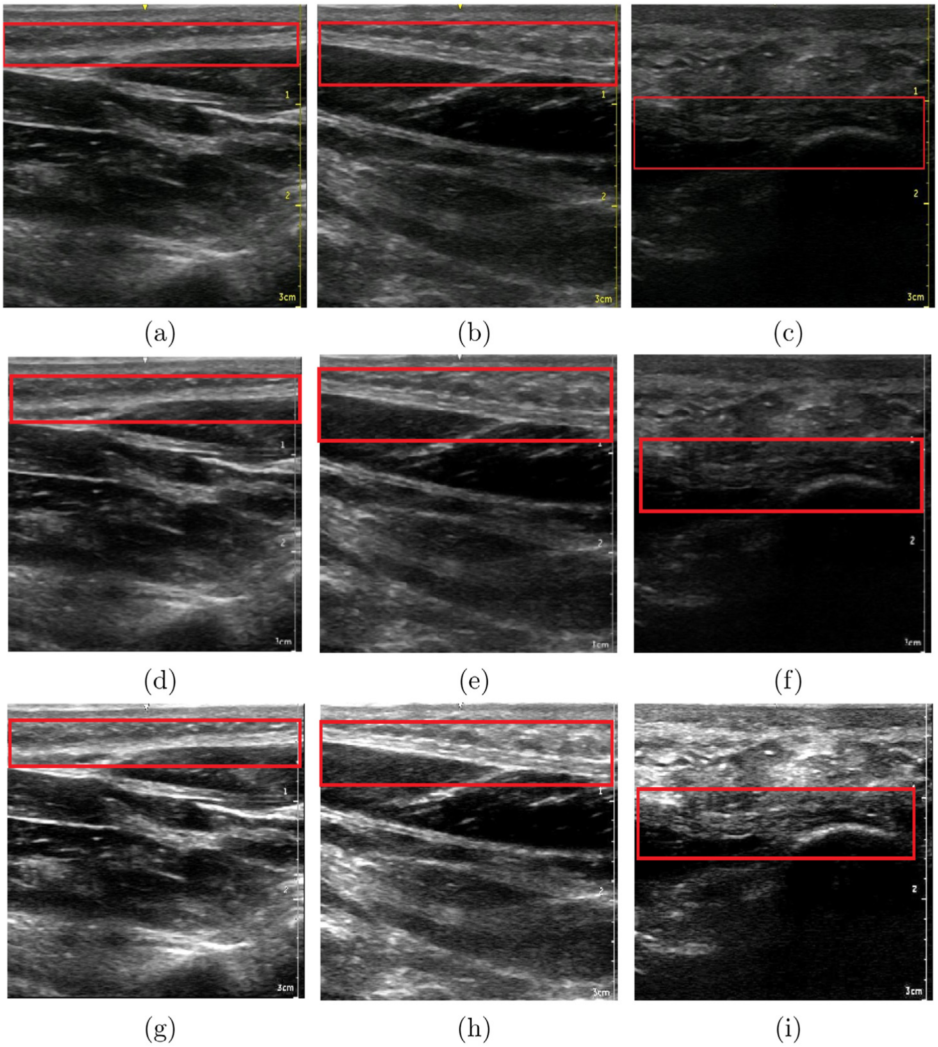

Fig. 9. Preprocessing results: (a)–(c) Original US images for different PF structures (Forefoot, Mid and Rear section). (d)–(f) Speckle reduction results using DT-CWT filter (reduces noise and improves the visual quality of the image). (g)–(e) Enhancement results using CLAHE filter (PF region has been enhanced and well defined).

where x, y denote the contour elements of C_{S_r} and $C_{R_{gt}}$, respectively, and $\|\cdot\|$ represents the Euclidean distance.

3.3. Establishing the ground truth inter-operator variability

Two medical experts, with different levels of experience (3–5 years), performed independent manual segmentation of the plantar fascia region (Fig. 6) and measured the thickness independently using each image. The datasets generated by the two experts were used to establish the ground truth values of the plantar fascia region thickness. Intra- and inter-operator variability was assessed using several metrics as presented in Table 1, with the two operators presenting very close results for all segmentation metrics used. Inter-operator variability of the PF thickness measurements was also assessed using a *t*-test and linear regression analysis, as reported in Table 1, indicating consistent reproducibility (Fig. 8).

3.4. Statistical comparison between manual and automatic segmentation

Three different statistical tests were performed to assess the validity of automatic segmentation methods in relation to manual measurements, including multiple regression analysis, repeated ANOVA test and post-hoc paired *t*-test in order to analyse the pairing between the PF thickness taken manually and the estimation methods, and to demonstrate that PF thickness varies along the sites of measurement. The alpha value for statistical significance was set at 0.025 based on a Bonferroni correction. All the statistical analyses were computed using GraphPad Prism Software version 7.01 (GraphPad Software, CA, USA).

4. Experimental results and discussion

Different experiments were performed to prove the capability of the proposed supervised ANN segmentation method including the preprocessing stage. Fig. 9 shows the results of applying the preprocessing methods using DT-CWT and CLAHE filters for despeckling and enhancement operations.

4.1. Feature selection and classification results

Feature selection analysis results of the 15 highest ranked predictors computed from 150 PF US images are shown in Table 2 and Fig. 10. For each feature, the weight predictor was computed and the features were assigned a rank order according to their predictor weights. The reason for feature ranking and selection analysis is to

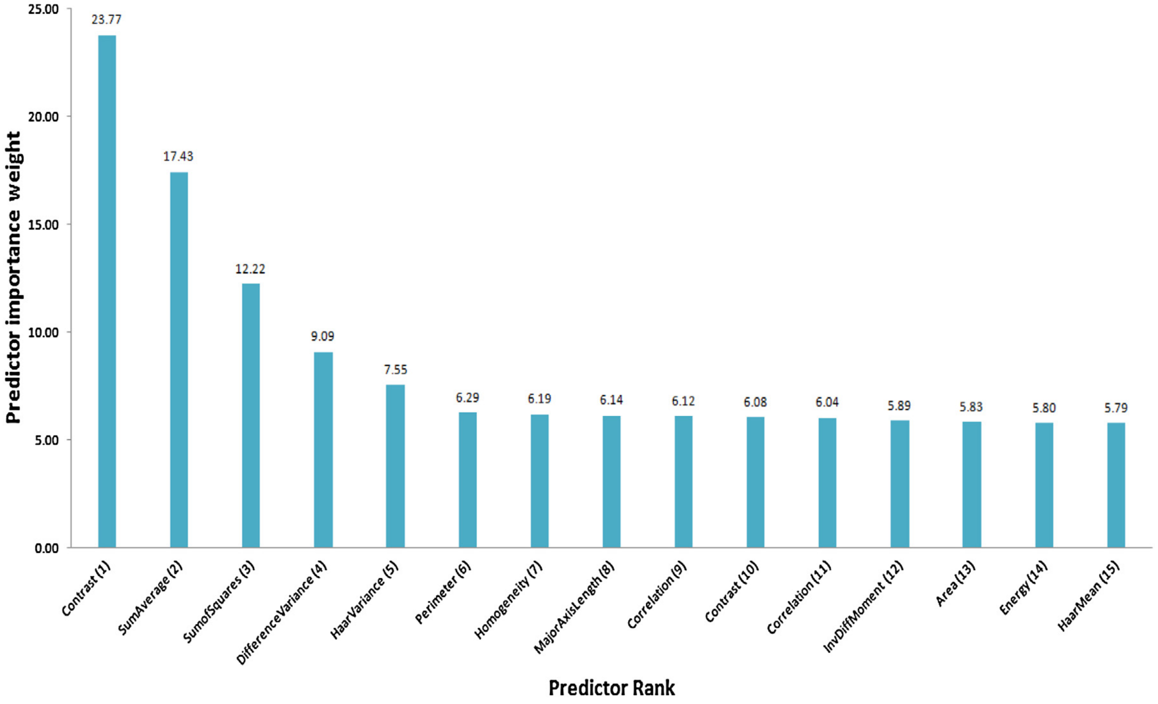

Fig. 10. A bar plot of ranked predictors (features importance) based on importance weights.

determine the best discriminatory features that define PF area and to eliminate similar or highly co-dependant features. It is clearly evident, from feature selection analysis results (Table 2 and Fig. 10), that the best 15 features were the ones with the highest ranked predictors (based on their importance weights) and which gave the best classification results. The main features included contrast, sum average, sum of squares and difference variance. The best result for RBF-NN classifier was also achieved with the best 15 selected feature set compared to other sets. The percentage of correctly classified PF segments was 98.80%. The performance measures of the RBF-NN classifier are shown in Table 3. The best result for RBF-NN classifier was achieved with the selected 15 feature set with a high mean accuracy of 98.75%, high mean TNR of 99.37% and low mean CE of 0.0182.

4.2. Segmentation results

The segmentation results are shown in Figs. 11–13 , and tabulated in Tables 4 and 5. Fig. 11 shows the segmented PF region results outlined manually by a physician (red contours) for different PF sites (Forefoot, Midfoor and Rearfoot sections), the segmentation results of the proposed method (green contours) using the RBF-NN classifier, and the binary mask of segmented PF region results. Fig. 12 shows the segmentation results (binary mask of segmented PF region) of the semi-automatic region based active contour (snakes) method (Kass et al., 1988), and Fig. 13 shows the segmentation results of localizing region based active contour (fully-automated) method (Lankton and Tannenbaum, 2008), as described previously. The segmentation results shown in Figs. 11–13 demonstrate that the proposed method correctly and

Table 4
Quantitative segmentation evaluation of the proposed method (Mean ± STD).

US images	Region-Based Metrics				Distance-Based Metrics	
	Precision (%)	Dice (%)	Sensitivity (%)	Specificity (%)	Hausdorff (mm)	MSSD (mm)
Image_Set 1	96.98 ± 1.43	97.69 ± 1.72	98.50 ± 1.05	98.90 ± 1.06	1.79 ± 1.66	0.11 ± 0.05
Image_Set 2	97.70 ± 1.33	97.78 ± 1.93	99.34 ± 0.66	98.79 ± 1.21	1.78 ± 0.57	0.20 ± 0.21
Image_Set 3	97.13 ± 1.87	97.29 ± 1.71	98.90 ± 1.10	97.99 ± 1.01	1.57 ± 0.42	0.31 ± 0.37
Image_Set 4	96.41 ± 1.75	96.61 ± 1.60	98.62 ± 1.06	97.49 ± 1.93	1.32 ± 0.25	0.10 ± 0.07
Image_Set 5	97.00 ± 1.13	97.81 ± 0.82	98.76 ± 0.58	98.48 ± 0.72	1.56 ± 0.60	0.28 ± 0.36
Image_Set 6	97.70 ± 1.20	98.43 ± 0.96	98.61 ± 1.43	98.43 ± 1.08	1.61 ± 0.89	0.22 ± 0.29
Mean ± STD	97.15 ± 0.49	97.60 ± 0.61	98.77 ± 0.32	98.38 ± 0.54	1.60 ± 0.17	0.20 ± 0.10

Table 5
Segmentation performance metrics of different segmentation methods and the proposed method (Mean ± STD).

Segmentation methods	Region-Based Metrics				Distance-Based Metrics	
	Precision (%)	Dice (%)	Sensitivity (%)	Specificity (%)	Hausdorff (mm)	MSSD (mm)
Lankton &Tannenbaum	76.73 ± 11.02	78.02 ± 9.89	75.67 ± 9.97	91.81 ± 5.35	3.00 ± 2.59	1.31 ± 0.30
Kass et al.	92.28 ± 7.14	81.21 ± 2.95	73.00 ± 5.93	96.58 ± 3.95	2.26 ± 0.18	1.45 ± 0.50
Proposed Method	97.15 ± 0.49	97.60 ± 0.61	98.77 ± 0.32	98.38 ± 0.54	1.60 ± 0.17	0.20 ± 0.10

Table 6
Thickness estimation by the proposed method for all different PF structures (Rearfoot, Midfoot and Forefoot sections).

Patients	Rearfoot PF section			Midfoot PF section			Forefoot PF section		
	Manual (mm)	Thick 1 (mm)	Thick 2 (mm)	Manual (mm)	Thick 1 (mm)	Thick 2 (mm)	Manual (mm)	Thick 1 (mm)	Thick 2 (mm)
Case 1	2.49 ± 0.030	2.82 ± 0.005	2.58 ± 0.011	1.55 ± 0.011	1.92 ± 0.002	1.67 ± 0.030	1.10 ± 0.010	1.14 ± 0.050	1.14 ± 0.019
Case 2	2.67 ± 0.033	3.07 ± 0.002	2.78 ± 0.030	1.61 ± 0.014	2.60 ± 0.033	1.73 ± 0.020	1.12 ± 0.010	1.64 ± 0.008	1.13 ± 0.007
Case 3	2.80 ± 0.040	2.99 ± 0.031	2.87 ± 0.020	1.87 ± 0.084	2.34 ± 0.001	2.01 ± 0.040	1.25 ± 0.030	1.54 ± 0.016	1.31 ± 0.004
Case 4	2.15 ± 0.020	2.38 ± 0.051	2.21 ± 0.010	1.81 ± 0.091	2.02 ± 0.004	1.87 ± 0.010	1.19 ± 0.050	1.76 ± 0.010	1.29 ± 0.023
Case 5	2.03 ± 0.040	3.00 ± 0.053	2.13 ± 0.030	1.58 ± 0.041	2.13 ± 0.022	1.63 ± 0.011	1.34 ± 0.040	1.51 ± 0.008	1.44 ± 0.011
Case 6	2.63 ± 0.040	2.24 ± 0.016	2.75 ± 0.040	1.62 ± 0.092	1.95 ± 0.005	1.69 ± 0.022	1.32 ± 0.040	1.67 ± 0.016	1.34 ± 0.001
Case 7	2.95 ± 0.027	2.47 ± 0.009	3.11 ± 0.012	1.80 ± 0.029	1.73 ± 0.034	1.94 ± 0.027	1.20 ± 0.025	1.51 ± 0.009	1.25 ± 0.014
Case 8	2.93 ± 0.015	2.41 ± 0.019	3.09 ± 0.008	1.75 ± 0.015	1.95 ± 0.002	1.90 ± 0.029	1.43 ± 0.016	1.30 ± 0.001	1.54 ± 0.007
Case 9	2.29 ± 0.041	2.36 ± 0.007	2.33 ± 0.033	1.51 ± 0.033	2.09 ± 0.018	1.57 ± 0.001	1.32 ± 0.040	1.95 ± 0.094	1.33 ± 0.004
Case 10	1.90 ± 0.035	3.17 ± 0.021	1.94 ± 0.002	1.71 ± 0.034	2.15 ± 0.009	1.76 ± 0.008	1.26 ± 0.020	1.55 ± 0.015	1.37 ± 0.022
Case 11	2.21 ± 0.036	2.50 ± 0.033	2.23 ± 0.019	1.81 ± 0.030	1.73 ± 0.012	1.89 ± 0.005	1.19 ± 0.040	1.49 ± 0.025	1.22 ± 0.004
Case 12	2.16 ± 0.045	2.82 ± 0.056	2.19 ± 0.013	1.88 ± 0.031	1.61 ± 0.030	1.96 ± 0.025	1.32 ± 0.017	1.58 ± 0.055	1.34 ± 0.011
Case 13	2.20 ± 0.041	2.86 ± 0.033	2.23 ± 0.039	1.53 ± 0.034	1.76 ± 0.009	1.57 ± 0.021	1.26 ± 0.041	1.76 ± 0.010	1.27 ± 0.005
Case 14	2.86 ± 0.042	2.82 ± 0.021	3.07 ± 0.043	1.70 ± 0.014	1.61 ± 0.031	1.89 ± 0.017	1.36 ± 0.050	1.58 ± 0.054	1.52 ± 0.014
Case 15	2.75 ± 0.035	3.19 ± 0.020	2.95 ± 0.031	1.73 ± 0.024	2.05 ± 0.012	1.90 ± 0.023	1.47 ± 0.032	1.50 ± 0.008	1.57 ± 0.009
Case 16	2.65 ± 0.065	3.74 ± 0.003	2.69 ± 0.043	1.68 ± 0.051	2.80 ± 0.081	1.74 ± 0.018	1.10 ± 0.020	2.34 ± 0.011	1.12 ± 0.001
Case 17	2.68 ± 0.052	2.22 ± 0.009	2.77 ± 0.061	1.58 ± 0.063	1.95 ± 0.001	1.64 ± 0.014	1.03 ± 0.080	1.39 ± 0.008	1.11 ± 0.001
Case 18	2.87 ± 0.043	2.66 ± 0.055	2.94 ± 0.005	1.71 ± 0.033	2.02 ± 0.008	1.76 ± 0.013	1.10 ± 0.010	1.38 ± 0.009	1.13 ± 0.005
Case 19	3.40 ± 0.044	2.46 ± 0.025	3.56 ± 0.014	1.81 ± 0.094	1.78 ± 0.008	1.92 ± 0.021	1.38 ± 0.050	1.56 ± 0.017	1.44 ± 0.023
Case 20	1.92 ± 0.025	3.17 ± 0.010	1.99 ± 0.007	1.52 ± 0.022	1.96 ± 0.002	1.59±0.009	1.15 ± 0.014	1.38 ± 0.009	1.18 ± 0.006
Case 21	2.14 ± 0.042	2.04 ± 0.033	2.17 ± 0.041	1.53 ± 0.011	1.84 ± 0.001	1.57 ± 0.001	1.27 ± 0.044	1.64 ± 0.022	1.31 ± 0.003
Case 22	2.43 ± 0.033	2.82 ± 0.056	2.50 ± 0.050	1.52 ± 0.021	1.77 ± 0.006	1.62 ± 0.005	1.30 ± 0.040	1.29 ± 0.015	1.38 ± 0.009
Case 23	2.92 ± 0.035	2.86 ± 0.022	2.99 ± 0.002	1.82 ± 0.033	1.82 ± 0.004	1.90 ± 0.006	1.25 ± 0.020	1.69 ± 0.002	1.28 ± 0.005
Case 24	2.62 ± 0.025	2.50 ± 0.021	2.67 ± 0.028	1.60 ± 0.014	1.73 ± 0.011	1.77 ± 0.15	1.27 ± 0.044	1.49 ± 0.025	1.32 ± 0.013
Case 25	2.59 ± 0.021	3.17 ± 0.008	2.65 ± 0.027	1.75 ± 0.007	2.15 ± 0.009	1.88 ± 0.18	1.18 ± 0.017	1.55 ± 0.015	1.26 ± 0.006
Range	1.90 - 3.40	2.04 - 3.74	1.94 - 3.56	1.51 - 1.88	1.61 - 2.80	1.57 - 2.01	1.03 - 1.47	1.14 - 1.76	1.11 - 1.57
RMSE	—	1.11	**0.43**	—	1.49	**0.49**	—	1.60	**0.28**

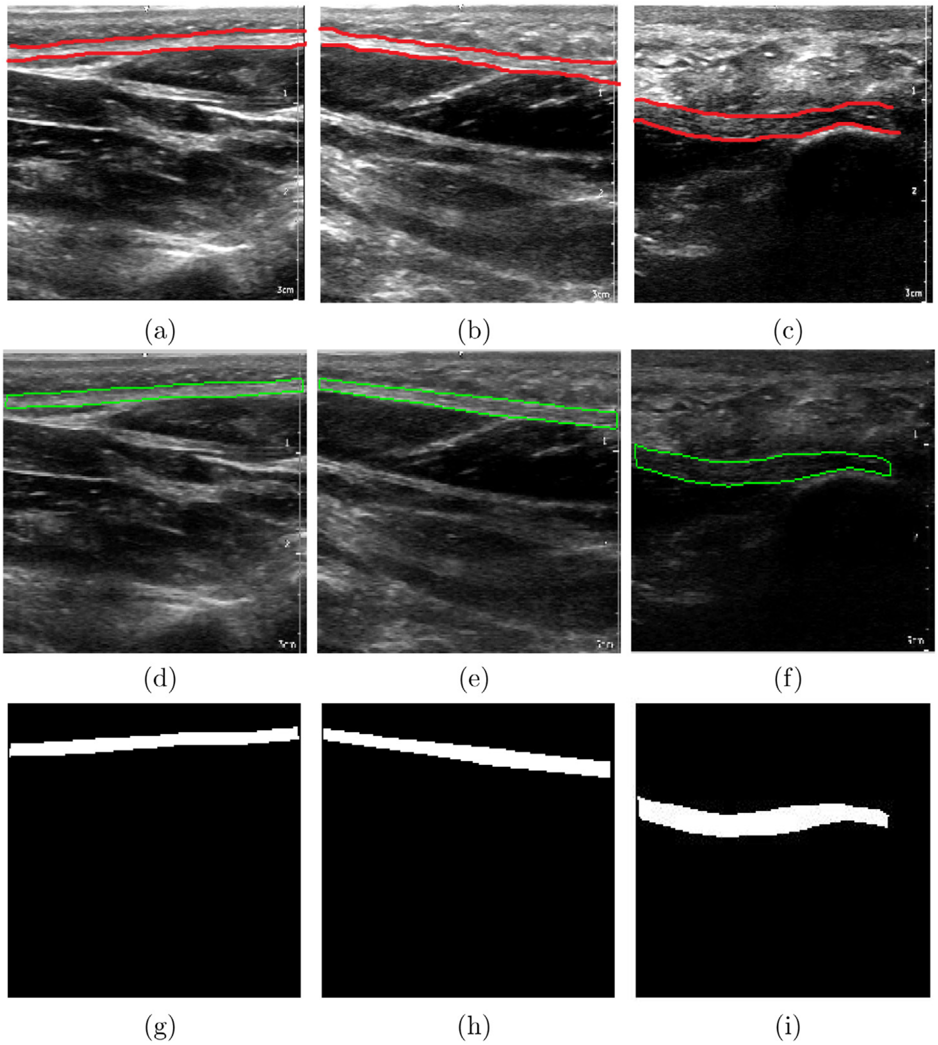
(a) (b) (c)
(d) (e) (f)
(g) (h) (i)

Fig. 11. Segmentation results of the proposed method. (a)–(c) PF region outlined manually by a physician (red contours). (d)–(f) Segmented PF region result produced by RBF-NN classifier (green contours). (g)–(i) Binary mask of segmented PF region results produced by RBF classifier.

precisely segments the PF area in all different structures compared to the selected active contour based methods.

Table 4 summarizes the quantitative segmentation results (mean ± STD) of the proposed method. The results of six different PF US image sets (25 US images per set) show that all obtained values were close to the ground truth values for both region based metrics and distance metrics (reported only in the PF US images where there were no failures). The ranges of overall means were 96–98% for precision, 96–99% for Dice similarity, 98–100% for sensitivity, 97–99% for specificity, 1 mm–2 mm for Hausdorff and 0.1 mm–0.2 mm for MSSD, with low standard deviation values, indicating better segmentation in terms of precision, Dice similarity, sensitivity and specificity (closer to 100% in similarity criteria), and low Hausdorff and MSSD values (closer to zero in similarity criteria) in the range 0 mm–15 mm and 0 mm–5 mm, respectively for effective segmentation results.

Table 5 compares the performance of the proposed method with the selected active contour based methods. From these results, it is evident that the proposed method exhibits the best performance in terms of all calculated segmentation metrics, with high mean values equal to 97.15% for precision, 97.60% for Dice similarity, 98.77% for sensitivity and 98.38% for specificity, and low mean values equal to 1.6 mm for Hausdorff distance and 0.2 mm for MSSD, with low standard deviation values. These results demonstrate the effectiveness of the proposed segmentation approach, with advantages over other methods. The active contour methods used in the evaluation and testing relied on variation information of edge intensity, and in most cases they are likely to miss certain parts of the PF region during the active contour segmentation process, leading to false segmentation of other objects in the image with similar intensity values to the PF region. This would require more processing steps, including despeckling, enhancement and morphological operations, such as opening, closing and filling (as shown in Figs. 12 and 13).

4.3. Thickness estimation results

Table 6 shows the automatic thickness estimation results using the two proposed methods (Thick 1 and Thick 2) for all different PF structures compared with manual measurements (established in Section 3.3). To demonstrate the significant positive relationship between the manual thickness measurements and the two automatic methods and that the thickness of the PF varies along its length, regression analysis, ANOVA and post-hoc *t*-test statistics were carried out. The results are presented in Tables 7 and 8. The regression analysis presented in Table 7 revealed a significant

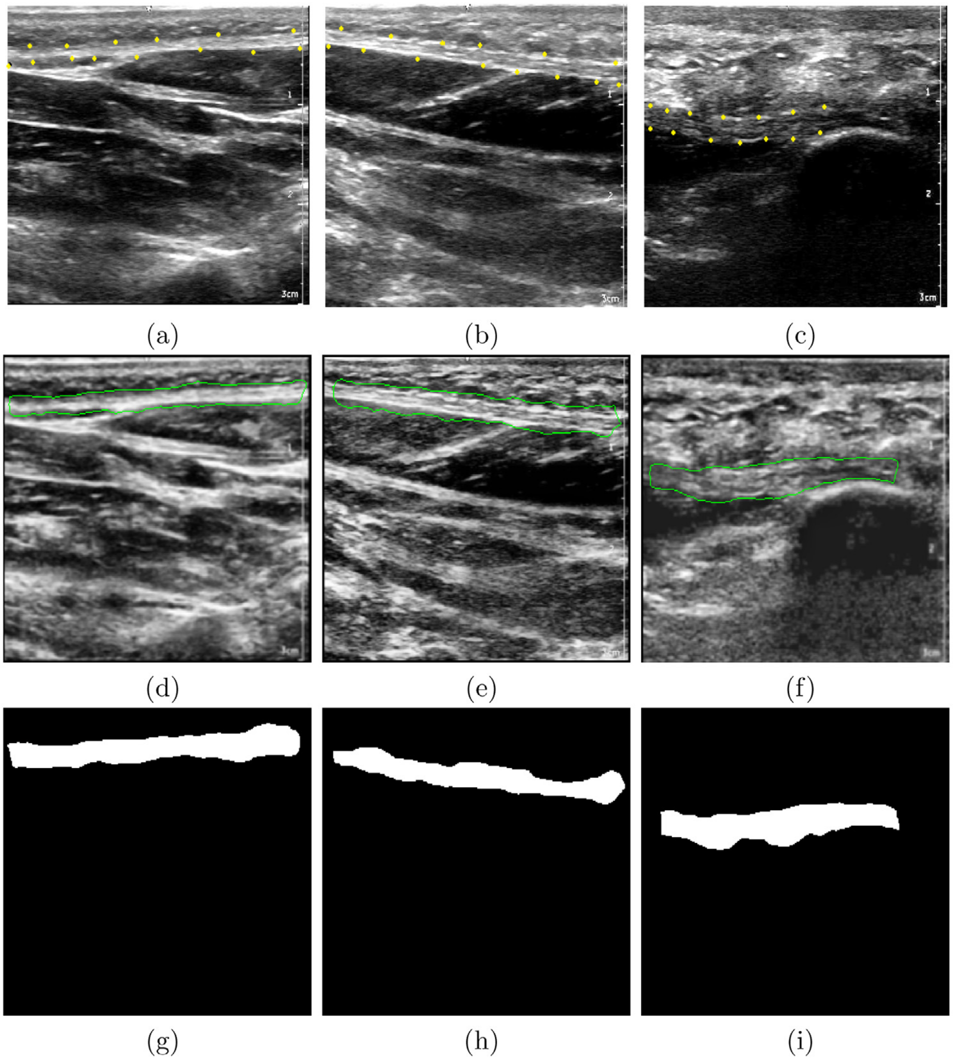

Fig. 12. Segmentation results of a semi-automatic region based active contour (snakes) method. (a)–(c) Active contour initialization using a manual snake mask initialization (red dots). (d)–(f) Preliminary active contour segmentation results (green contours).(g)–(i) Final selected PF region.

Table 7
Regression analysis between manual and automatic assessment of PF thickness.

Different sites of PF	Rearfoot		Midfoot		Forefoot	
Thickness calculation methods	Thick 1	Thick 2	Thick 1	Thick 2	Thick 1	Thick 2
Multiple regression (R^2)	0.1116	0.9947	0.06648	0.9516	0.03744	0.9603
***P*-value**	0.2976	<0.0001	0.3761	<0.0001	0.4295	<0.0001
Significant pairing with manual?	No	Yes	No	Yes	No	Yes

positive pairing between manual measurement and the automatic Thick 2 method for all PF measurement sites ($R^2 = 0.995$, $R^2 = 0.952$ and $R^2 = 0.960$ for rearfoot, midfoot and forefoot, respectively, $p < 0.0001$). However, there was no significant positive relationship between manual measurement and Thick 1 method ($p > 0.05$). The results of the ANOVA test presented in Table 8 distinguished between different PF sites using the three different methods; $F = 189.5$ was obtained for manual measurements, and 159.7 for Thick 2, showing comparable results. All three approaches distinguished between the different sites, $p < 0.0001$. The repeated paired post-hoc *t*-test revealed a significant difference between different PF sites in all thickness calculation methods (manual, Thick 1 and Thick 2), $p < 0.0001$. The results presented here show that thickness values obtained using the second automatic method (Thick 2) were closer to the ground truth thickness values than the first method (Thick 1). In addition, the statistical analysis showed that the PF thickness varies along its length. The overall estimated PF thickness using the second method ranged from approximately 1.94 mm–3.56 mm for the rearfoot section, 1.57 mm–2.01 mm for the midfoot section, and 1.11 mm–1.57 mm for the forefoot section. Thus, the proposed method is advantageous and reliable in quantifying PF thickness in different structures anatomically located in the rearfoot, midfoot and forefoot sections.

5. Conclusion

It can be argued that while general methods for US image segmentation are lacking, segmentation processes tend to be application dependent. In the field of PF segmentation, no automatic segmentation methods have been developed to date, and this

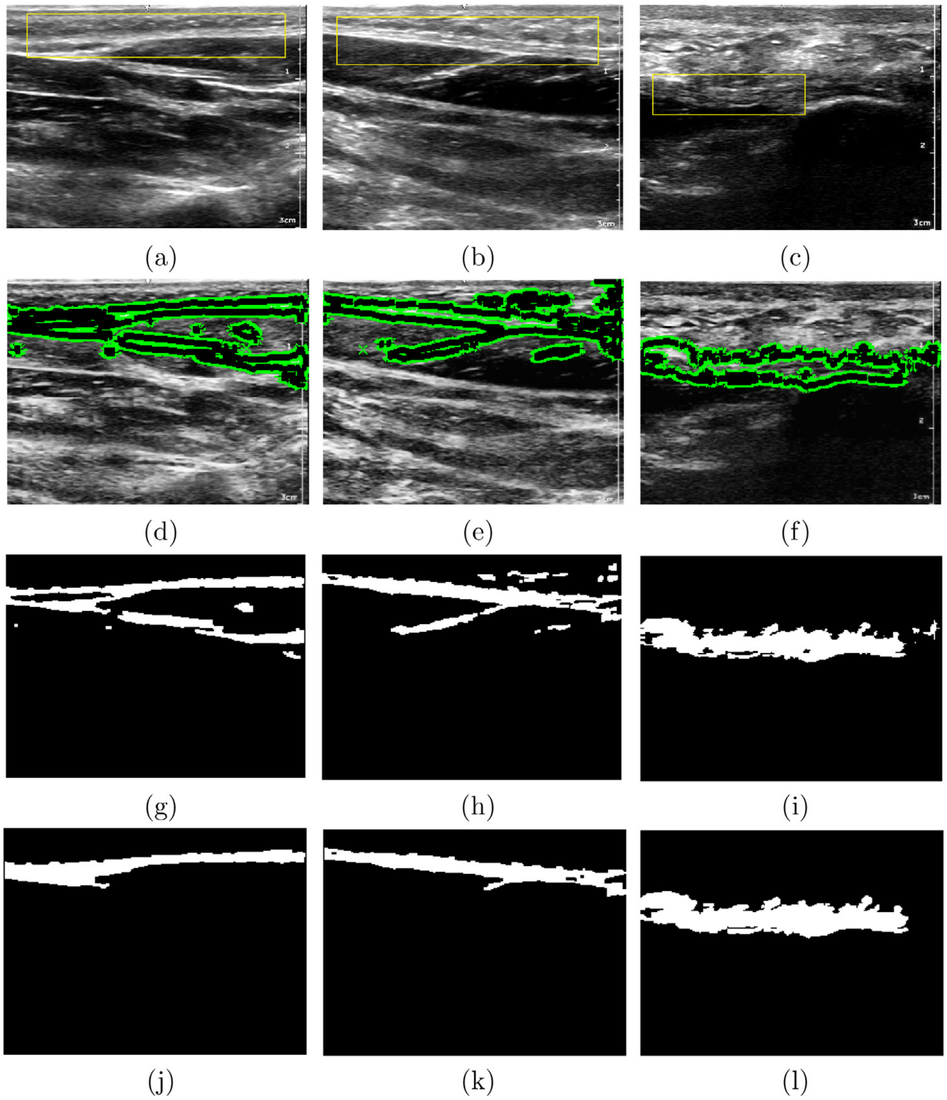

Fig. 13. Segmentation results of a fully automatic localizing region based active contour method. (a)–(d) Predefining the initial mask. (d)–(f) Active contour initialization using a predefined initial mask. (g)–(i) Preliminary region based segmentation results. (j)–(l) Final results using morphological operations such as: opening, closing, thresholding, and region filling.

Table 8
ANOVA analysis of differences between manual and automatic measurements.

Thickness estimation method	Manual	Thick 1	Thick 2
F	189.5	93.26	159.7
P-**value**	<0.0001	<0.0001	<0.0001
Difference between sites?	Yes	Yes	Yes

makes the task of segmenting PF US images in the clinic more challenging; however, this also presents an opportunity for developing novel methods to facilitate this task for clinicians. The method presented in this study used a segmentation approach with feature extraction, ranking, selection analysis and RBF-NN classifier to automatically segment the PF area and estimate its thickness. The proposed segmentation method obtained favourable results compared to other active contour methods reported in the literature. Performance evaluation showed that the proposed automatic method can successfully segment the PF region and estimate the PF thickness from US images. Such a segmentation application is not only able to significantly reduce the time required by physicians for PF pathology diagnosis, but can also reduce the subjectivity that accompanies manual delineations and thickness measurements, further assisting pathologists by facilitating early diagnosis. It is evident from the statistical analysis that the second method (Thick 2) outperforms the first method (Thick 1) in terms of significant positive pairing between the manual and automatic assessment. In addition, the findings indicate a significant difference between PF structures, strongly suggesting that the thickness of the PF varies along the length of the foot. The effectiveness of the proposed method supports the potential of its use in US imaging. However, further investigation is required to (i) evaluate the performance of the proposed model in a larger dataset of normal and abnormal US images against measurements by a larger number of experts, (ii) analyse its impact on medical applications by using different ultrasound machines with advanced specifications, and (iii) improve the segmentation process such that it can classify different PF US images into normal, medium and abnormal sets.

References

Akfirat, M., Sen, C., Günes, T., 2003. Ultrasonographic appearance of the plantar fasciitis. Clin. Imag. 27 (5), 353–357.
Angin, S., Crofts, G., Mickle, K.J., Nester, C.J., 2014. Posture Ultrasound evaluation of foot muscles and plantar fascia in *Pes planus*. Gait Posture 40, 48–52.

Bishop, C.M., 2006. Pattern Recognition and Machine Learning. Springer, New York, USA.

Blum, H., 1967. A transformation for extracting new descriptors of dhape. In: Wathen-Dunn, W. (Ed.), Models for the Perception of Speech and Visual Form. MIT Press, Cambridge, MA, USA, pp. 362–380.

Borş, A.G., Pitas, I., 1996. Median radial basis function neural network. IEEE Trans. Neural Netw. 7 (6), 1351–1364.

Borş, A.G., Pitas, I., 1999. Object classification in 3-d images using alpha-trimmed mean radial basis function network. IEEE Trans. Image Process. 8 (12), 1744–1756.

Broomhead, D.S., Lowe, D., 1988. Radial basis functions, multi-variable functional interpolation and adaptive networks. Tech. rep., Royal Signals and Radar Establishment, Memorandum No. 4148, London, UK.

Chan, T., Vese, L., 2001. Active contours without edges. IEEE Trans. Image Process. 10 (2), 266–277.

Chang, C.-Y., Lei, Y.-F., Tseng, C.-H., Shih, S.-R., 2010. Thyroid segmentation and volume estimation in ultrasound images. IEEE Trans. Biomed. Eng. 57 (6), 1348–1357.

Chang, R., 2010. Plantar fasciitis: Biomechanics, atrophy and muscle energetics (PhD dissertation). University of Massachusetts Amherst, USA.

Chang, S., Yu, B., Vetterli, M., 2000. Adaptive wavelet thresholding for image denoising and compression. IEEE Trans. Image Process. 9 (9), 1532–1546.

Cheng, J.-W., Tsai, W.-C., Yu, T.-Y., Huang, K.-Y., 2012. Reproducibility of sonographic measurement of thickness and echogenicity of the plantar fascia. J. Clin. Ultrasound 40 (1), 14–19.

Chun, Y.D., Seo, S.Y., Kim, N.C., 2003. Image retrieval using BDIP and BVLC moments. IEEE Trans. Circuits Syst. Video Technol. 13 (9), 951–957.

Crofts, G., Angin, S., Mickle, K.J., Hill, S., Nester, C.J., 2014. Reliability of ultrasound for measurement of selected foot structures. Gait Posture 39 (1), 35–39.

Deshpande, R., Ramalingam, R., Chockalingam, N., Naemi, R., Branthwaite, H., Sundar, L., 2013. An automated segmentation technique for the processing of foot ultrasound images. 2013 IEEE Eighth International Conference on Intelligent Sensors, Sensor Networks and Information Processing, 380–383.

Di Stefano, L., Bulgarelli, A., 1999. A simple and efficient connected components labeling algorithm. In: 1999. Proceedings. International Conference on Image Analysis and Processing. IEEE, pp. 322–327.

Dice, L.R., 1945. Measures of the amount of ecologic association between species. Ecology 26 (3), 297–302.

Fabrikant, J.M., Park, T.S., 2011. Plantar fasciitis (fasciosis) treatment outcome study: plantar fascia thickness measured by ultrasound and correlated with patient self-reported improvement. Foot 21 (2), 79–83.

Ganzalez, R.C., Woods, R.E., 2002. Digital Image Processing, 2nd ed. Prentice-Hall, Englewood Cliffs, NJ, USA.

Gonzalez, R., Woods, R., 2011. Digital Image Processing. Pearson Education Asia, India.

Gonzalez, R., Woods, R., Eddins, S., 2010. Digital Image Processing Using MATLAB. Tata McGraw Hill Education, Private Limited, New Delhi, India.

Ham, F.M., Kostanic, I., 2000. Principles of Neurocomputing for Science and Engineering, 1st Edition. McGraw-Hill Higher Education, Private Limited, New Delhi, India.

Haralick, R.M., Shanmugam, K., Dinstein, I.H., 1973. Textural features for image classification. IEEE Trans. Syst. Man Cybern. SMC-3 (6), 610–621.

Heimann, T., Van Ginneken, B., Styner, M., Arzhaeva, Y., Aurich, V., Bauer, C., Beck, A., Becker, C., Beichel, R., Bekes, G., et al., 2009. Comparison and evaluation of methods for liver segmentation from ct datasets. IEEE Trans. Med. Imag. 28 (8), 1251–1265.

Huang, C.-K., Kitaoka, H.B., An, K.-N., Chao, E.Y., 1993. Biomechanical evaluation of longitudinal arch stability. Foot Ankle Int. 14 (6), 353–357.

Kass, M., Witkin, A., Terzopoulos, D., 1988. Snakes: active contour models. Int. J. Comput. Vis. 1 (4), 321–331.

Kelikian, A.S., 2012. Sarrafian's Anatomy of the Foot and Ankle: Descriptive, Topographic, Functional. Lippincott Williams & Wilkins, Philadelphia, USA.

Kingsbury, N., 1998. The dual-tree complex wavelet transform: a new technique for shift invariance and directional filters. In: Proceeding of the 8th IEEE DSP Workshop, Utah. Vol. 8. Citeseer, p. 86.

Kingsbury, N., 1999. Shift invariant properties of the dual-tree complex wavelet transform. Proceedings of the 1999 IEEE International Conference on Acoustics, Speech and Signal Processing, vol. 3.

Kwong, P., Kay, D., Voner, R., White, M., 1988. Plantar fasciitis. mechanics and pathomechanics of treatment. Clin. Sports Med. 7 (1), 119–126.

Lankton, S., Tannenbaum, A., 2008. Localizing region-based active contours. IEEE Trans. Image Process. 17 (11), 1–11.

Moody, J., Darken, C.J., 1989. Fast learning in networks of locally-tuned processing units. Neural Comput. 1 (2), 281–294.

Noble, J.A., Boukerroui, D., 2006. Ultrasound image segmentation: A survey. IEEE Trans. Med. Imag. 25 (8), 987–1010.

Orr, M.J.L., 1996. Introduction to Radial Basis Function Networks.

Park, J.W., Yoon, K., Chun, K.S., Lee, J.Y., Park, H.J., Lee, S.Y., Lee, Y.T., 2014. Long-term outcome of low-energy extracorporeal shock wave therapy for plantar fasciitis: Comparative analysis according to ultrasonographic findings. Ann. Rehabil. Med. 38 (4), 534–540.

Pizer, S.M., Amburn, E.P., Austin, J.D., Cromartie, R., Geselowitz, A., Greer, T., ter Haar Romeny, B., Zimmerman, J.B., Zuiderveld, K., 1987. Adaptive histogram equalization and its variations. Comput. Vis. Graphics Image Process. 39 (3), 355–368.

Pope, J.A., 1999. Medical Physics: Imaging. Heinemann Advanced Science. Pearson Education Limited, Harlow, UK.

Roffo, G., Melzi, S., Cristani, M., 2015. Infinite feature selection. 2015 IEEE International Conference on Computer Vision (ICCV), 4202–4210.

Rubinstein, R.Y., 1997. Optimization of computer simulation models with rare events. Eur. J. Oper. Res. 99 (1), 89–112.

Rueda, S., Fathima, S., Knight, C.L., Yaqub, M., Papageorghiou, A.T., Rahmatullah, B., Foi, A., Maggioni, M., Pepe, A., Tohka, J., Stebbing, R.V., McManigle, J.E., Ciurte, A., Bresson, X., Cuadra, M.B., Sun, C., Ponomarev, G.V., Gelfand, M.S., Kazanov, M.D., Wang, C.-W., Chen, H.-C., Peng, C.-W., Hung, C.-M., Noble, J.A., 2014. Evaluation and comparison of current fetal ultrasound image segmentation methods for biometric measurements: a grand challenge. IEEE Trans. Med. Imag. 33 (4), 797–813.

Saber, N., Diab, H., Nassar, W., Razaak, H.A., 2012. Ultrasound guided local steroid injection versus extracorporeal shockwave therapy in the treatment of plantar fasciitis. Alexandria J. Med. 48 (1), 35–42.

Selesnick, I., Baraniuk, R., Kingsbury, N., 2005. The dual-tree complex wavelet transform. IEEE Signal Process. Mag. 22 (6), 123–151.

Sendur, L., Selesnick, I., 2002. Bivariate shrinkage functions for wavelet-based denoising exploiting interscale dependency. IEEE Trans. Signal Process. 50 (11), 2744–2756.

Shih, F., 2009. Image Processing and Mathematical Morphology: Fundamentals and Applications. CRC Press, Taylor & Francis, Boca Raton, USA.

Sokolova, M., Lapalme, G., 2009. A systematic analysis of performance measures for classification tasks. Inf. Process. Manag. 45 (4), 427–437.

Szabo, T.L., 2013. Diagnostic Ultrasound Imaging: Inside Out. Biomedical Engineering. Elsevier Science Academic Press, Cambridge, Massachusetts, USA.

Telea, A., 2014. Data Visualization: Principles and Practice, 2nd ed. Taylor & Francis, Milton Park, Abingdon, UK.

Udupa, J.K., Leblanc, V.R., Zhuge, Y., Imielinska, C., Schmidt, H., Currie, L.M., Hirsch, B.E., Woodburn, J., 2006. A framework for evaluating image segmentation algorithms. Comput. Med. Imaging Graph. 30 (2), 75–87.

Umbaugh, S., 2005. Computer Imaging: Digital Image Analysis and Processing. A CRC Press Book. Taylor & Francis, Milton Park, Abingdon, UK.

Wearing, S.C., Smeathers, J.E., Sullivan, P.M., Yates, B., Urry, S.R., Dubois, P., 2007. Plantar fasciitis: are pain and fascial thickness associated with arch shape and loading? Phys. Ther. 87 (8), 1002–1008.

Wearing, S.C., Smeathers, J.E., Yates, B., Sullivan, P.M., Urry, S.R., Dubois, P., 2004. Sagittal movement of the medial longitudinal arch is unchanged in plantar fasciitis. Med. Sci. Sports Exerc. 36 (10), 1761–1767.

Wen, X., Yuan, H., Yang, C., Song, C., Duan, B., Zhao, H., 2007. Improved haar wavelet feature extraction approaches for vehicle detection. In: Intelligent Transportation Systems Conference, ITSC 2007, IEEE, pp. 1050–1053.

Weszka, J.S., Dyer, C.R., Rosenfeld, A., 1976. A comparative study of texture measures for terrain classification. IEEE Trans. Syst. Man Cybern. SMC-6 (4), 269–285.

Zuiderveld, K., 1994. Graphi gems IV. In: Contrast limited adaptive histogram equalization. Academic Press Professional, Inc., San Diego, CA, USA, pp. 474–485.